

Supplement for: Empirical attribution of a drying Himalayan river through remote sensing and secondary data

Gopal Penny^{1,2}, Zubair A. Dar³, and Marc Müller^{1,2}

¹Environmental Change Initiative, University of Notre Dame, Indiana, USA

²Civil and Environmental Engineering and Earth Sciences, University of Notre Dame, Indiana, USA

³Energy and Resources Group, University of California, Berkeley, California, USA

Contents

Section S1: Streamflow separation and integrity checks

- Figure S1: Pairwise double mass curves for streamflow
- Figure S2: Intraannual baseflow

Section S2: Precipitation interpolation

- Figure S3: Water balance with elevation-gradient precipitation interpolation

Section S3: ET regression analysis

Section S4: Additional figures

- Figure S4: Mosaic land cover
- Figure S5: Open water extent
- Figure S6: Pre-2000 clear-sky summer images
- Figure S7: Water extent versus flow at Sangam station
- Figure S8: Permafrost likelihood

S1 Streamflow separation and integrity checks

To ensure reliability of data from each stream gauge, we prepared pairwise double-mass plots between gauges using median streamflow from each month and finding that all gauges were consistent with at least one adjacent gauge (see Figure S1). To further ensure temporal and spatial consistency, we sampled three

observations per month for each gauge, selected to be evenly spaced throughout the month. Using this dataset, we conducted baseflow separation using a numerical filter (Nathan and McMahon, 1990) and then aggregated baseflow, quickflow, and total streamflow to monthly, seasonal, and annual values. The baseflow separation calculated from trimonthly streamflow compared well with baseflow from daily streamflow (OLS $R^2 = 0.72$, slope = 0.87) and, importantly, ensured temporal consistency across all gauges. Finally, we calculated subcatchment streamflow at each gauge by subtracting streamflow from the gauge directly upstream. The full results are presented in Figure S2.

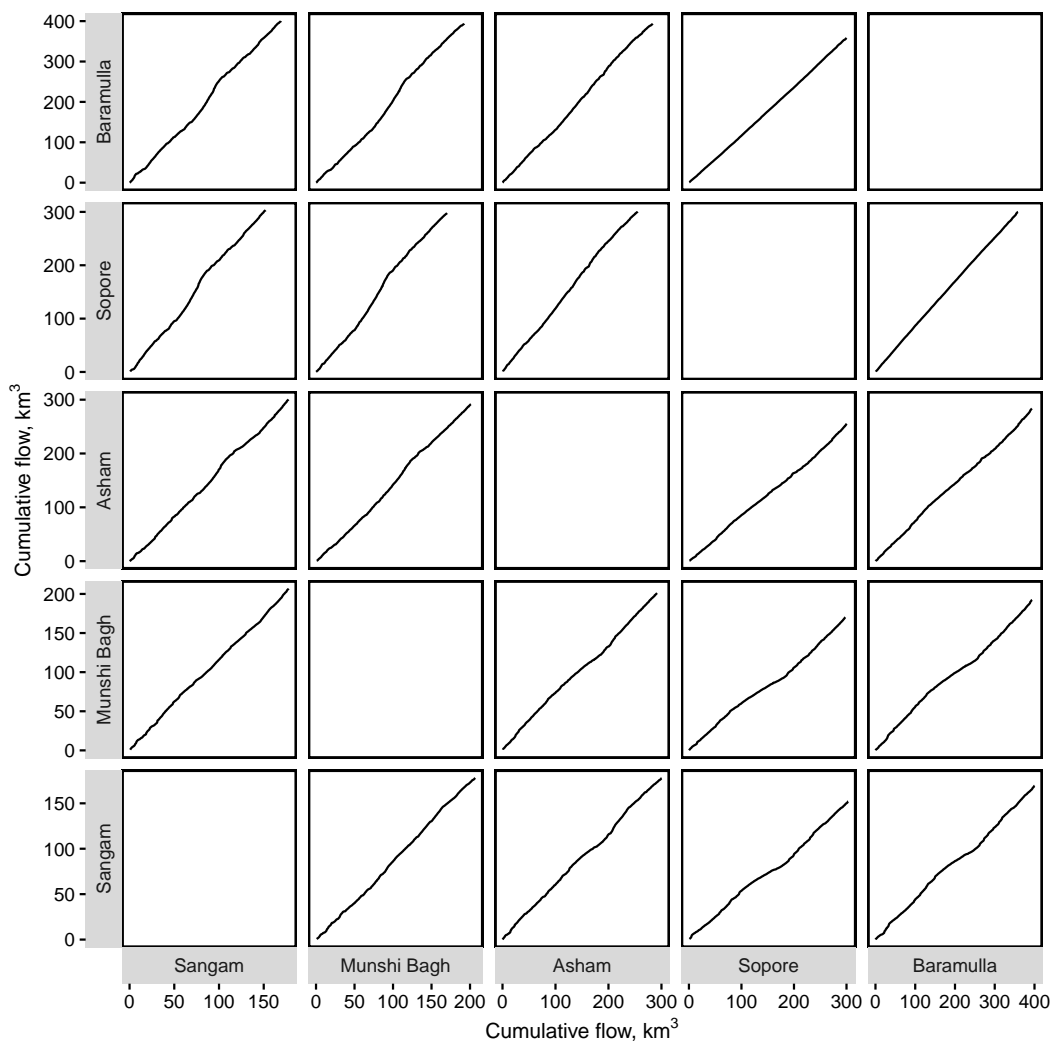


Figure S1: Pairwise double mass curves for median monthly streamflow across each of the 5 gauges from 1960 through 2013. Each gauge compares well with the neighboring gauge, with the order from downstream to upstream being Baramulla–Sopore–Asham–Munshi Bagh–Sangam.

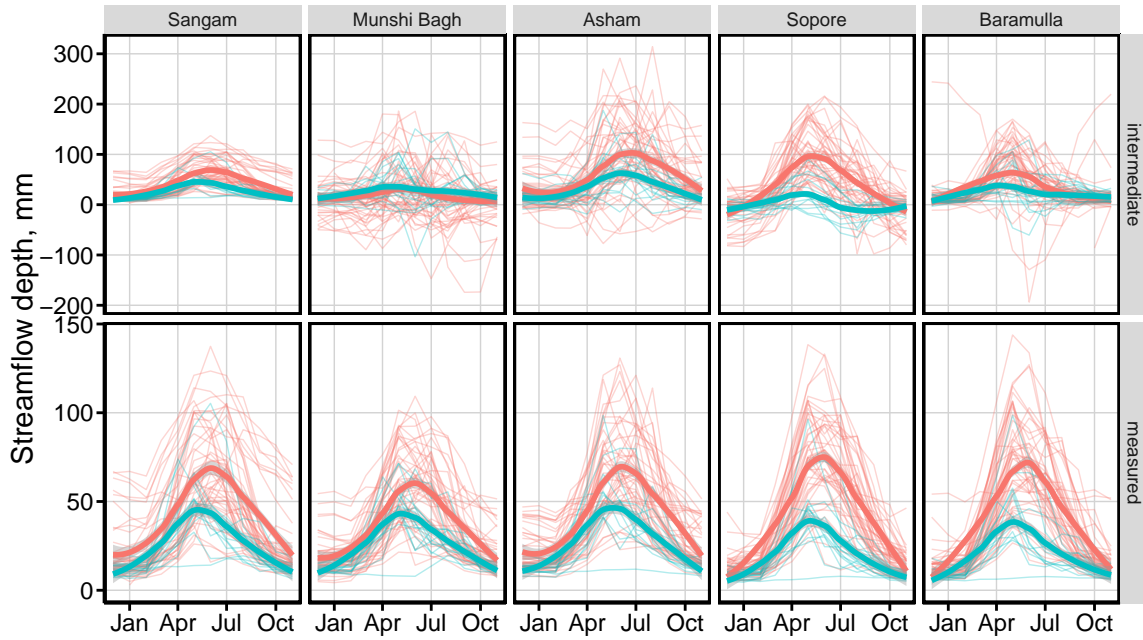


Figure S2: Intraannual baseflow at all five gauges before (red) and after (blue) 2000. Observations for all years are included in thin, semi-transparent lines, with the smoothed average shown in thicker dark lines. The figure includes baseflow calculated at each gauge (“measured,” bottom) and the that calculated as inflow from the “immediate” subcatchment of the gauge (calculated by subtracting baseflow at the upstream gauge, top).

S2 Precipitation interpolation

As an alternative to Thiessen polygons, we also applied an elevation gradient with inverse-distance weighting to regionalize gauged precipitation. To determine basin precipitation using an elevation gradient, we first fit linear precipitation-elevation curves for each year-season combination using ordinary least-squares regression. We then determined a pre-2000 and post-2000 elevation gradient, taken as the mean elevation gradient within each season. As a robustness check, we ran t-tests to determine if the difference in means was statistically significant. For instance, the pre-2000 summer elevation gradient was 0.29 mm m^{-1} compared to a gradient of 0.17 mm m^{-1} for the post-2000 summer period, with the t-test indicating a statistically significant difference ($p = 0.23$). The remaining seasons did not exhibit a statistically significant difference in the elevation gradient. However, we ultimately decided to use the (more parsimonious) Thiessen interpolation because it better captures the net outgoing fluxes of the water balance (i.e., streamflow plus ET) before (-14%) and after ($+16\%$) 2000. In contrast, the elevation gradient approach overestimated these fluxes considerably ($+43\%$ and $+93\%$, respectively). We therefore take the Thiessen interpolation as a more reliable approach for estimating watershed precipitation.

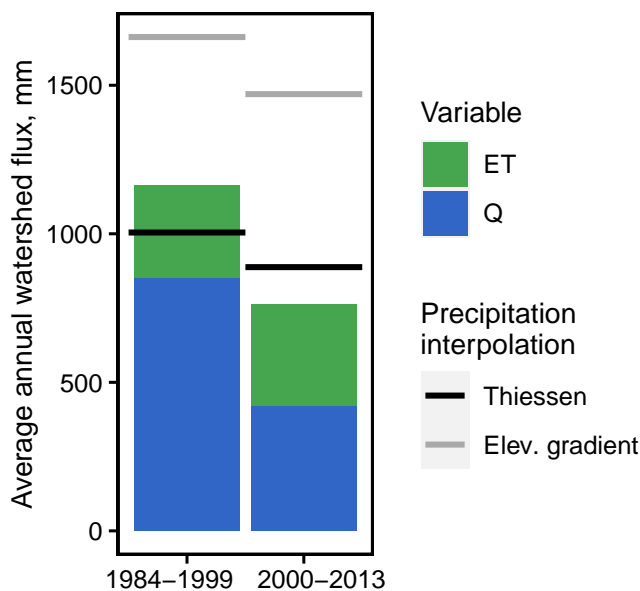


Figure S3: Average annual water balance in the Upper Jhelum including both type of precipitation interpolation: Thiessen polygon and elevation gradient.

S3 ET regression analysis

The ET regression was run on 500 m pixels sampled on a 2.5 km grid to determine a_s , after which ET was predicted for all Landsat pixels at 480 m. To conduct the analysis, multiple satellite products were prepared

and downloaded from Google Earth Engine, including 500 m MODIS ET and 480 m pyramid pixels of Landsat 5 and 7 NDVI calculated from surface reflectance. Both products were sampled on the same 2.5 km grid. Although the pixels did not perfectly align, the processing speed was increased dramatically by sampling Landsat pixels at 480 m rather than reprojecting and resampling Landsat to the MODIS resolution. Furthermore, the correlation of Landsat NDVI between the MODIS resolution and the 480 m sampling was high ($R^2 = 0.94$).

Temperature data was obtained from IMD-Srinagar at Pahalgam (monthly), Srinagar (daily), Qazigund (daily), and Gulmarg (daily) stations. We interpolated temperature across the watershed using inverse-distance weights and applied seasonal adiabatic lapse rates to adjust for elevation differences (see Dodson and Marks, 1997; Stahl et al., 2006, for details). Lapse rates ranged from 6.12 °C/km in winter to 8.58 °C/km in spring and were close to expected ranges for the climate and latitude (Stone and Carlson, 1979).

We determined the a_s and c coefficients using observations from the 2.5 km grid and nonlinear least-squares regression. The NDVI exponent was fit to $c = 0.81$, giving confidence in the regression and the diminishing relationship between NDVI and stomatal conductance at high NDVI. Evapotranspiration was then predicted for all 480 m Landsat pixels directly from Eq. 2 (main text) using long-term seasonal averages of NDVI before and after 2000.

S4 Additional Figures

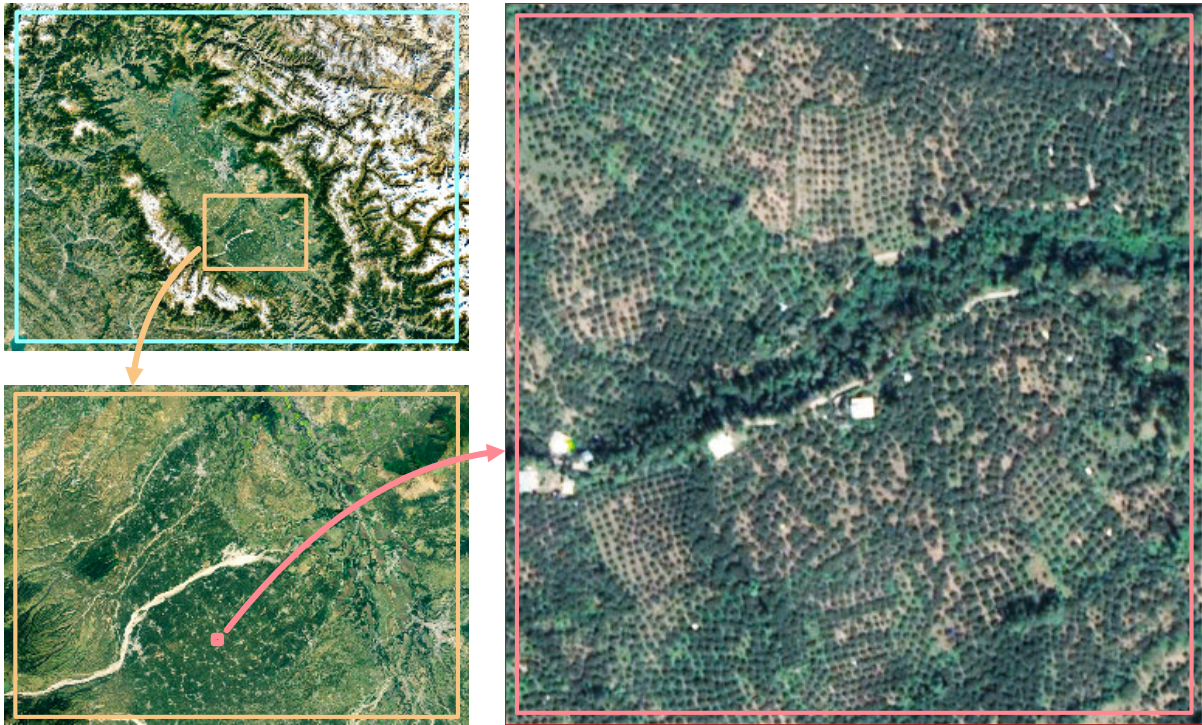


Figure S4: Visual inspection of satellite imagery from Google Earth (©2021 Google, ©2021 Maxar Technologies) in the southern portion of the Upper Jhelum confirms that the MODIS land use classification of mosaic vegetation represents orchards, seen throughout the right image as gridded sowing of trees.

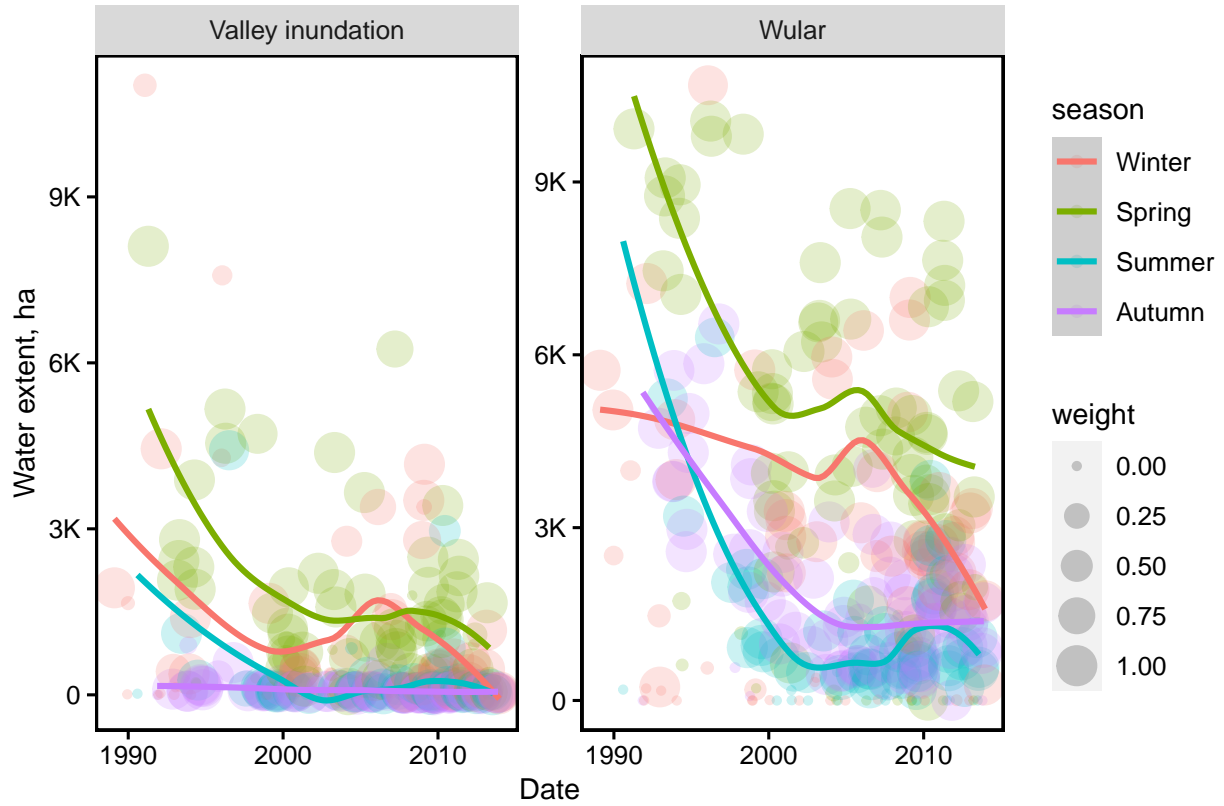


Figure S5: Open water extent classified from Landsat 5 and 7 imagery declined across all four seasons in Wular Lake and as exhibited by valley inundation. The curves are determined using locally estimated scatterplot smoothing (LOESS) regression. We gave more credibility to images in which there the cloud area was small in comparison to the water area, and therefore weighted individual observations by the ratio of the area of clouds over the area of water as $\exp(-A_{clouds}/A_{water})$.

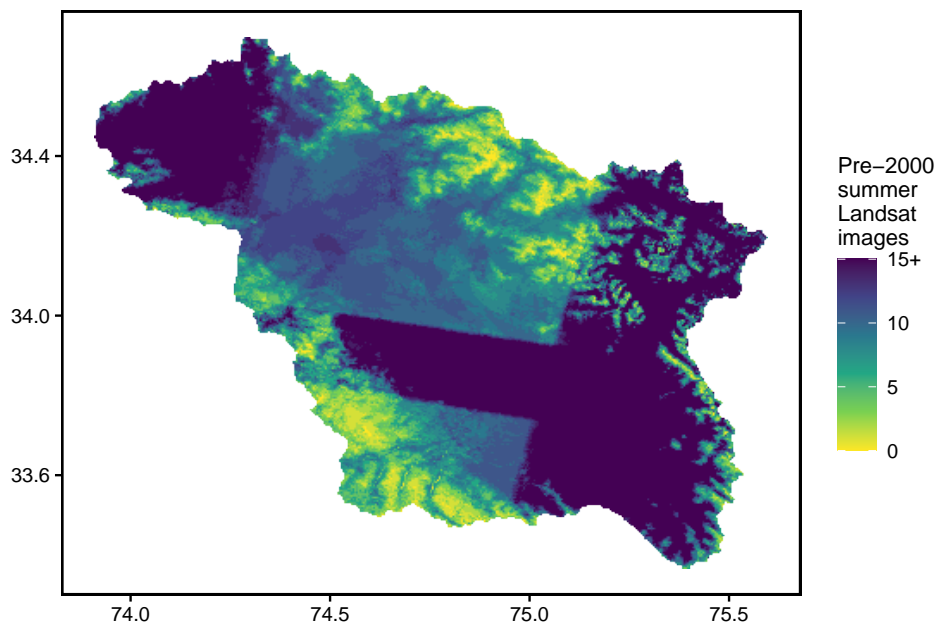


Figure S6: Number of pre-2000 clear-sky summer images at each pixel throughout the Upper Jhelum watershed. Higher elevations are more likely to be hidden by clouds and therefore be captured in fewer images.

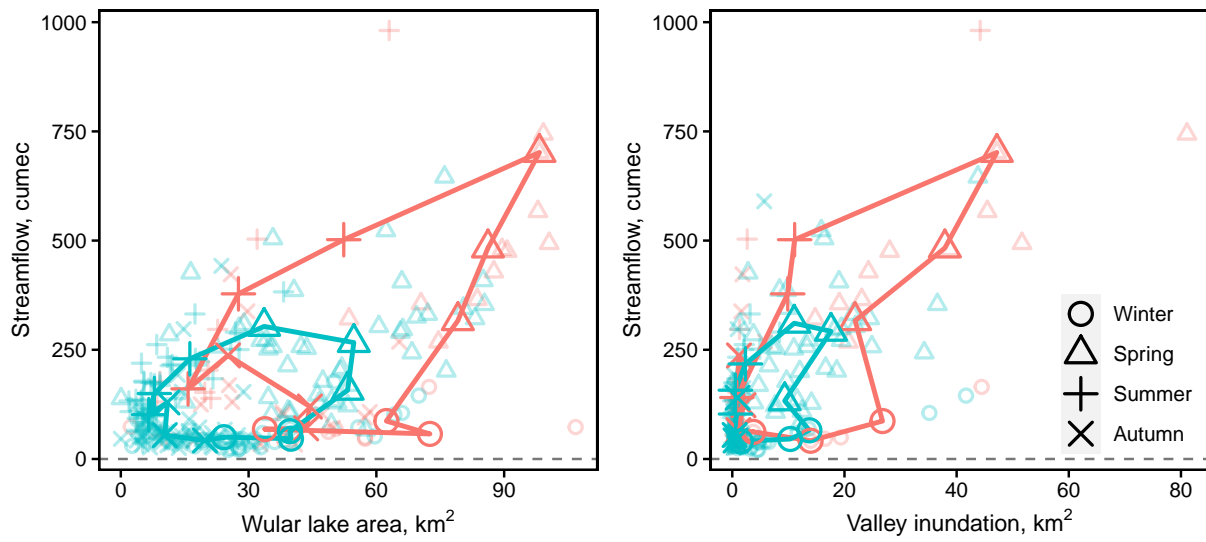


Figure S7: Water extent versus flow at Sangam station for Wular lake (left) and valley inundation (right), before (red) and after (blue) 2000. Each observation is shown as a small, semi-transparent marker. Monthly averages are presented in large markers connected by lines. The top-right triangle (in red, both sides) represents May, followed by the first summer month (June).

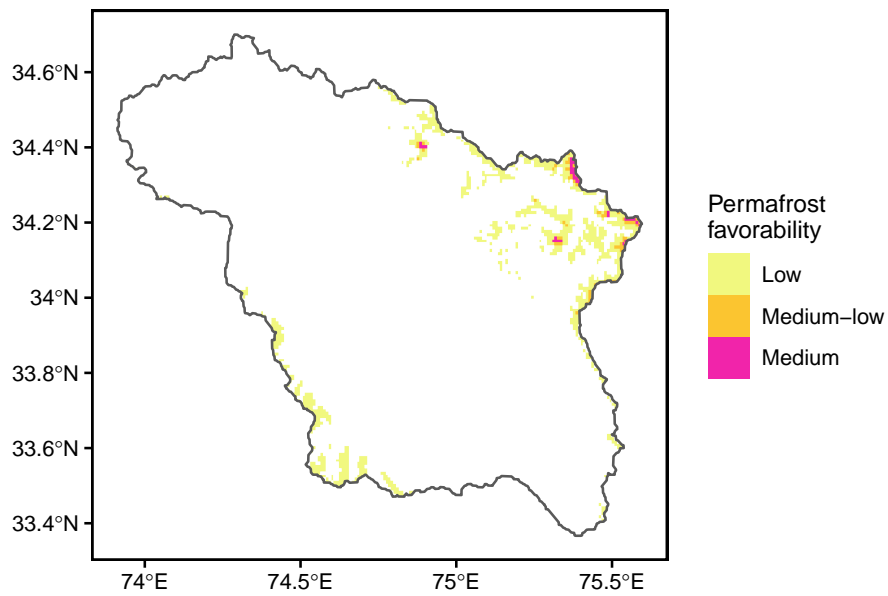


Figure S8: Permafrost likelihood from the Global Permafrost Zonation Index (Gruber, 2012). The index spans a range from a minimum of “permafrost exists only in most favorable conditions” and to a maximum of “permafrost exists in nearly all conditions.” We binned this scale into five groups of permafrost likelihood including low, medium-low, medium, medium-high, and high. The highest permafrost likelihood in the Upper Jhelum watershed is medium.

References

- Dodson, R. and Marks, D.: Daily air temperature interpolated at high spatial resolution over a large mountainous region, *Climate Research*, 8, 1–20, <https://doi.org/10.3354/cr008001>, 1997.
- Gruber, S.: Derivation and analysis of a high-resolution estimate of global permafrost zonation, *The Cryosphere*, 6, 221–233, 2012.
- Nathan, R. J. and McMahon, T. A.: Evaluation of Automated Techniques for Baseflow and Recession Analysis, *Water Resources Research*, 26, 1465–1473, <https://doi.org/10.1029/WR026i007p01465>, 1990.
- Stahl, K., Moore, R. D., Floyer, J. A., Asplin, M. G., and McKendry, I. G.: Comparison of approaches for spatial interpolation of daily air temperature in a large region with complex topography and highly variable station density, *Agricultural and Forest Meteorology*, 139, 224–236, <https://doi.org/10.1016/j.agrformet.2006.07.004>, 2006.
- Stone, P. H. and Carlson, J. H.: Atmospheric lapse rate regimes and their parameterization., *Journal of the Atmospheric Sciences*, 36, 415–423, [https://doi.org/10.1175/1520-0469\(1979\)036<0415:ALRRAT>2.0.CO;2](https://doi.org/10.1175/1520-0469(1979)036<0415:ALRRAT>2.0.CO;2), 1979.